European Journal of Mechanics B/Fluids 50 (2015) 89–97

Contents lists available at ScienceDirect

European Journal of Mechanics B/Fluids

journal homepage: www.elsevier.com/locate/ejmflu

The formation of coherent structures within turbulent fountains in stratified media

Daniel Freire *, Sandra Kahan, Cecilia Cabeza, Gustavo Sarasúa, Arturo C. Marti

Instituto de Física, Universidad de la República, Montevideo, Uruguay

ARTICLE INFO

Article history:
Received 2 September 2013
Received in revised form
10 September 2014
Accepted 10 November 2014
Available online 21 November 2014

Keywords:
Turbulent fountain
Instability
Coherent structures

ABSTRACT

An experimental investigation into the interaction between a turbulent fountain and its stratified environment is presented. A heavy fluid, cold water, is injected vertically upwards into a linearly stratified medium. As revealed by visualisations, the heavy-fluid jet reaches a maximum height before it begins to fall under to the effect of gravity. Due to fluid mixing and entrainment, the vertical momentum and the density of the jet fluid decrease as it submerges to an intermediate height of zero buoyancy. Large coherent structures are identified using Proper Orthogonal Decomposition (POD) on Digital Particle Image Velocimetry (DPIV) measurements. Experimental values of the main components of temporal and spatial spectra are compared to predictions based upon the dispersion relations for stratified media.

1. Introduction

The dynamical behaviour of fluids within stratified media presents a problem of considerable interest across a number of fields. Two different situations can be distinguished when a flow from a localised source is released into a stratified media [1]. In the case referred to as a *plume*, the buoyancy force acting on a fluid particle is in the same direction as that of the particle velocity. In the other case, when the fluid is moving in the opposite direction to the buoyant force, the flow is referred to as a *fountain*. Buoyancy and mixing effects are the dominant mechanisms that regulate the evolution of the fountain, although the fluid viscosity and boundary conditions should be neglected even though their effects are much smaller.

Understanding the dynamics of plumes is crucial for many environmental and pollution problems, such as the transport of contaminants, and plumes have therefore received considerably more attention than fountains. There are, however, a number of relevant applications for fountains [2], for instance selective withdrawal, desalination plants and the replenishment of magma chambers. In particular, an important technological application of turbulent fountains is the Selective Inverted Sink (SIS) [3,4] device. The main purpose of this device is to mitigate frost damage in agriculture, a problem that can have significant impacts on food production worldwide.

The main purpose of SIS is to prevent the onset of so-called radiation frosts, particularly the case of late frosts, as these may result in considerable economic losses due to crop failure [5]. In the presence of a radiation frost, air temperature is seen to increase with altitude (up to a few tenths of metres from the ground). In this case the atmosphere can be represented as a vertical succession of strata (horizontal layers of atmospheric air) of increasing temperature. The coldest air is deposited near the soil, potentially damaging crops. The relation between low temperatures and plant tissue damage has been extensively reported in agriculture literature (see for example [6,7]). It is found that below a critical temperature the exposure time required to severely damage crops decreases considerably. In this context, therefore, the effective control of temperature in cultivated areas is crucial.

Several strategies may be adopted to reduce damages resulting from radiation frosts, such as wind machines, man-made fog, the use of heaters or irrigation. Another approach is the commercially available SIS device, which operates through the selective withdrawal of the densest (coldest) air layer. The device has numerous advantages such as high efficiency, low pollution (both environmental and noise) and low maintenance [8]. Its operation is based on the dynamics of a fountain that is injected vertically from the ground into a less dense atmosphere. Understanding the fluid mechanisms of a fountain operating in a stratified medium is therefore of considerable interest.

This work is focused on the dynamics of a fountain, composed of water ejected from the bottom of a container into a medium with less dense (hotter) water. As the cold fluid rises, fluid from the less dense atmosphere is entrained [9]. The fountain fluid

* Corresponding author.
E-mail address: dfreire@fisica.edu.uy (D. Freire).
URL: http://fluidos.fisica.edu.uy (D. Freire).

http://dx.doi.org/10.1016/j.euromechflu.2014.11.009
0997-7546/

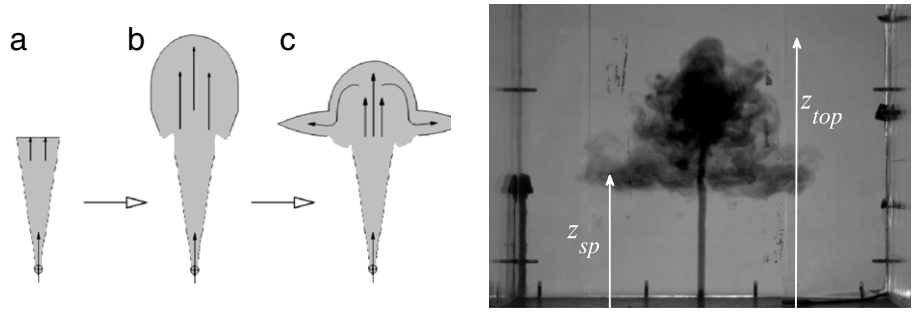

Fig. 1. Typical evolution of a fountain: scheme of the velocity field (left). Initially, the ejected fluid spreads (a), then, momentum of the rising fluid decreases as a result of the opposing buoyancy (b) and, finally, intrudes into the environment (c). Snapshot of the fully developed fountain with dye visualisation (right).

density decreases as it rises and, under the effect of gravity, reaches an initial zero-momentum height, z^i_{top}. The top of the fountain oscillates about this mean height, z_{top}. It is worth mentioning that the behaviour of z_{top} in the case of uniform surroundings was studied by G.R. Hunt et al. [10–12]. As the zero-momentum height oscillates the fluid begins to fall laterally until it reaches the bottom of the tank, if the atmosphere is homogeneous, or until it reaches an intermediate height if the atmosphere is linearly stratified. This height, z_{sp} is called the *height of spreading* or *intrusion height*, because it is where the fluid spreads radially. Fig. 1 outlines the typical evolution of a fountain as described above. In Fig. 1(b), the maximum height is reached and the flow begins to fall, while in Fig. 1(c) the fluid begins to spread radially at the intrusion height [13]. In a previous paper [14], the effects that turbulent fluctuations have on the behaviour of a fountain were described.

Here we analyse the dynamics of turbulent fountains using the technique of Proper Orthogonal Decomposition (POD), an effective method for identifying dominant features and events in experimental [15–17] and simulated data [18]. Although not applied in this work, it is noteworthy that recently P.J. Schmid [19] has recently developed the Dynamic Mode Decomposition (DMD) technique to capture the principal features of numerical and experimental data in fluids, as a complement to POD analysis. The DMD method can identify regions of localised instability, characterising their dynamical behaviour using a single frequency. POD allows the effective compression of large quantities of data such that the most useful information about the physical processes occurring may be extracted. In recent years, POD has begun to be used widely as a technique for identifying not only the dominant features in flows – coherent structures – but also for constructing low-dimensional models able to describe the principal flow dynamics using the smallest number of modes. In addition, several authors have used this technique as a filter tool on Digital Particle Image Velocimetry (DPIV) data, enabling them to identify structures based on the size of their spatial or temporal extent in the flow, for example eddy scales [17]. Cenedese & Monti [20,21] identified convective or vortex-like structures in a land- and sea-breeze circulation, under a calm stable environment, from the velocity fields under POD decomposition. Kostas et al. [16] applied this method to generate vorticity fields from velocity fields on a 2-D DPIV realisation in a backward-facing step flow. They compared vorticity decomposition with the curl of velocity decomposition, suggesting that the first technique is more effective.

The aim of this study is twofold, firstly to simulate the behaviour of a fountain in a stratified environment for two different inlet jets, and secondly to investigate the fluid dynamics of the fountain using the POD technique. The organisation of this paper is as follows. The experimental setup is described in the next section. The mathematical background explaining the POD fundamentals is presented in Section 3. The analysis of the results is detailed in Section 4. The study includes the main features of the obtained spatial POD modes, like predominant structures and the retained energy, as well as the energy distribution along different modes and their evolution in time, and the relation between them and dispersion relations for internal gravity waves. Finally, the conclusions are presented in Section 5.

2. Experimental setup

The experimental setup consists of a tank whose external walls are rectangular acrylic panes with dimensions 1.5 cm × 40 cm × 50 cm. Water is injected through a circular nozzle of 0.8 cm-diameter, located in the centre of the container floor, with a stable flow-rate of 0.30 L min^{-1} at the inlet. The flow rate is controlled by means of a valve and a flow metre with a full-scale accuracy of 1%.

The fluid within the container is water with a linear temperature–height profile, with the layer closest to the bottom of the container fixed at 15 °C and the fluid near the top wall at 27.5 °C. These temperatures are kept constant during the experiment using an external water cooling circuit on the bottom plate and an electrical heater on the top wall. To obtain the linear stratification, intermediate water layers were carefully heated by means of a sliding resistance. The density profile of the resulting stratified medium was allowed sufficient time (ca. 2 h) to stabilise, and the container was insulated with 10.0 cm deep panes of expanded polystyrene. Thermocouples were installed every 10 cm along two vertical borders of the container, to monitor the temperature gradient of the water volume. Fig. 2 displays a typical temperature profile obtained at the laboratory after de-stratification. A jet of water at 15 °C is injected through the inlet port of the base plate. Differing degrees of turbulence are generated using a stainless-steel woven wire mesh screen placed at the inlet port. Two configurations are studied, these being with unrestricted flow at injection point (referred to as *free*), and with an 80-mesh screen with wire diameter of 0.18 mm placed transversally at the jet inlet (referred to as *grid*) [14]. Two different techniques were employed to analyse the flow dynamics, namely visualisation using dye as a marker and DPIV measures. A set of ten visualisations were used to identify the main characteristics of the flow and also to measure the maximum and intrusion heights. DPIV experiments were performed three times and twice for the free and grid configurations, respectively.

Digital Particle Image Velocimetry [22,23] was used to determine the velocity fields. Both the environmental and the injected fluids are seeded with 50 μm diameter spherical polyamide particles. The fluid is illuminated with a 500 mW green laser sheet of 2.0 mm thickness. Images were captured by a CMOS camera at 4 fps and processed in Matlab using the open-source package OpenPIV [24,25]. To measure the motion of small groups of particles the code performs a cross-correlation between frames in which the image is divided and then displaced in order to find a maximum correlation. In our analysis the windows were chosen to be 64×64 pixels with a maximum displacement of 8 pixels. After performing each

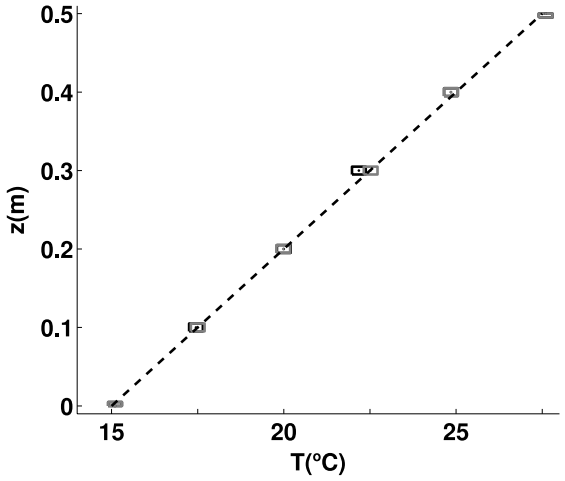

Fig. 2. An example of the temperature profiles obtained in the experiments after stratification. In black and grey are plotted values measured by the thermocouples in two different vertical borders of the container and the corresponding errors. The continuous line represents the ideal target temperature profile.

realisation, $M = 395$ frames for free and grid cases were digitalised resulting in a resolution of $N = (900 \times 1100)$ pixels. The size of the acquisition area is 27 cm $\times$ 30 cm and images were taken every 0.25 s. With this setup, the upper limit of the velocity that can be measured is about 1 cm/s. This condition is fulfilled everywhere except in the portion near the inlet of the jet, which was excluded in the DPIV analysis.

3. Proper Orthogonal Decomposition characterisation

This section is devoted to explain the mathematical background behind the POD technique. The definition of its main characteristic parameters is given in Section 3.2.

3.1. Mathematical background

Proper Orthogonal Decomposition, also known as Karhunen–Loève decomposition [26], is a powerful and elegant method of data analysis able to obtain accurate low-dimensional approximated descriptions of high-dimensional processes. To understand the fundamentals of the technique let us consider a sequence of observations represented by the scalar function $u(\vec{r}_i, t_j)$, for instance a component of the velocity field, sampled at pixel coordinates $\vec{r}_i$, with $i = 1, 2, \ldots, N$, at discrete times t_j, with $j = 1, 2, \ldots, M$.

A singular value decomposition in this matrix provides an optimal 2-norm variance decomposition,

$$u(\vec{r}_i, t_j) = \sum_{k=1}^{k_{\max}} \lambda_k \Phi_k(\vec{r}_i) \xi_k(t_j), \tag{1}$$

where $\lambda_1 > \lambda_2 > \cdots > \lambda_{\min(N,M)}$ are the ordered component weights of the expansion terms, and $\Phi_k(\vec{r}_i)$ and $\xi_k(t_j)$ the spatial and temporal orthonormal eigenmodes, respectively.

The sum indicated in the last equation can be truncated at $k_{\max} < \min(N, M)$. The advantage of POD is that it provides an optimal approximation with respect to other possible sets of orthonormal functions, since the average least-squares truncation error is minimum for any given number of basis functions, with $k_{\max} < \min(N, M)$. It is worth noting that due to the resolution of the images and the frame rate of the digital camera, the maximum possible value for $k_{\max}$ is equal to $M = \min(N, M)$ in our experiments. For each time t_j, the time-dependent amplitudes of the k-modes are defined as,

$$a_k(t_j) = \lambda_k \xi_k(t_j), \tag{2}$$

which modulate the normalised spatial eigenfunctions $\Phi_k(\vec{r}_i)$.

3.2. POD characterisation

To characterise the dynamics of the system, POD can be applied to the velocity fields obtained by DPIV. In particular, the eigenvalues sum can be associated with the total energy of the system [27] using the expression,

$$E = \sum_{k=1}^{M} \lambda_k^2, \tag{3}$$

and also with the relative energy e_k retained by the k-mode,

$$e_k = \frac{\lambda_k^2}{\sum_{k=1}^{M} \lambda_k^2}. \tag{4}$$

In addition to the spectra, the entropy of the data set provides useful information about the dynamics of the system,

$$S = -\lim_{M \to \infty} \frac{1}{\ln M} \sum_{k=1}^{M} e_k \ln e_k, \tag{5}$$

where $\ln M$ is a normalisation factor.

Another method with which to describe the degree of disorder related to turbulent fluctuations in the flux [28] is the so called Karhunen–Loève dimension (KLD_h). This represents the number of linear eigenvalues needed to approximate a fraction of the total energy ($0 < h < 1$), and is given by,

$$KLD_h = \max \left\{ p : \frac{\sum_{k=1}^{p} \lambda_k^2}{\sum_{k=1}^{M} \lambda_k^2} \leq h \right\}. \tag{6}$$

This quantity also gives information about the spectral distribution e_k.

It is also useful to analyse the distribution of the relative energy contained in the velocity field. The cumulative energy stored at the $k_{\max}$ first modes at time t_j, relative to the energy summed over the full set of modes and over the total time of the experiment, is defined as,

$$E(t_j, k_{\max}) = \frac{\sum_{k=1}^{k_{\max}} a_k^2(t_j)}{\sum_{j=1}^{M} \sum_{k=1}^{N} a_k^2(t_j)}. \tag{7}$$

Note that for the case $k_{\max} = M$ we obtain the total kinetic energy retained by the full assembly of modes, $E(t_j, M)$; the energy of a given mode k at time t_j is $E_k(t_j) = a_k^2(t_j)$.

4. Results

In the previous section it was shown how POD provides a method to compare different experimental conditions with the smallest amount of information. The following sections are devoted to discussing the characteristics of the first modes, which capture the principal features of the system.

Experiments with two configurations under different jet inlet conditions, namely free and grid inlets as described in Section 2, were performed. The main features of the flow, these being the initial, stationary and intrusion (or spreading) heights, are measured by means of dye visualisation. Due to the inherent oscillations of these quantities their mean values are computed and the error is taken to be the standard deviation of the measurements. The results summarised in Table 1 correspond to

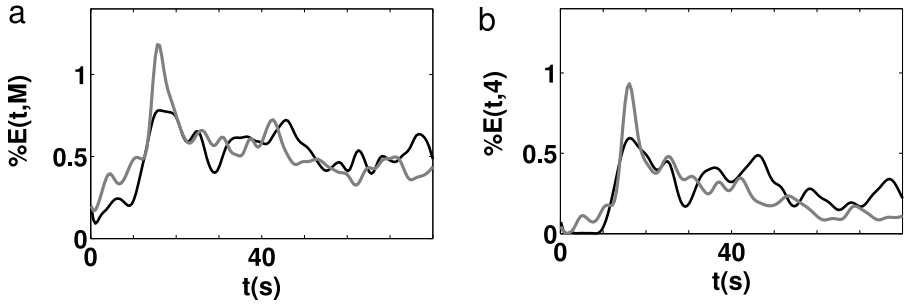

Fig. 3. Temporal distribution of the percentage of cumulative energy stored in the full set of M modes (a) and only for the four first modes (b). The black and grey lines represent the measurements for the free and grid configurations, respectively.

Table 1
Measurements obtained from experiments with dyed fluid. The columns correspond to the maximum height reached at the initial stage (z^i_{top}), the mean value of the maximum height reached by the fountain at the stationary stage (z_{top}) and the mean value of the spreading height also at the stationary stage (z_{sp}).

Configuration	z^i_{top} (cm)	z_{top} (cm)	z_{sp} (cm)
Free	28	27 ± 1	16 ± 2
Grid	27	25 ± 1	14 ± 3

Table 2
Main parameters obtained from POD analysis: total energy of the system (E), relative energy of the three first modes (e_1, e_2 and e_3), entropy (S), and KLD_h for half of the total energy ($h = 0.5$).

Configuration	E	e_1	e_2	e_3	S	$KLD_{0.5}$
Free	12.1	0.1794	0.0540	0.0364	0.790	22
Grid	30.4	0.1247	0.0469	0.0245	0.859	39

one measurement of each configuration (free and grid), but they are representative due to the high reproducibility of the results (some of the realisations both using ink to visualise or employing the DPIV technique are shown in the supplementary material Appendix A).

The measured heights are greater for the free inlet than for the grid configuration. From the fluctuations of the fountain top and spreading heights it can be also surmised that the effects of turbulent fluctuation are higher on the grid configurations [14].

The characterisation obtained from the visualisations can be extended by calculating the energy, entropy and KLD_h defined at Section 3.2, these being displayed in Table 2. We notice that in the free inlet measurement the first energy mode is the largest, and the total energy, the entropy and the KLD_h are all smaller than the corresponding values obtained from the grid inlet measurement. As a consequence, the former flow is more ordered than the last one. The effect of the attached arrays at the inlet is to increase the turbulent fluctuations. In particular, as shown in Section 4.2, the first energy mode is related to the radial spreading of the flow.

4.1. Accuracy

The temporal distribution of the energy allows additional insight into the fluid dynamics for both experimental conditions. The first modes recover the main features of the fountain, and if further modes are added it is possible to reproduce the characteristics associated with its turbulent behaviour in more detail. To verify that the four first modes reproduce the main features of the flow for the whole experiment, in Fig. 3 we plot the temporal distribution of cumulative energy, $E(t_j, k_{\max})$, for both configurations. As it can be seen, the grid configuration energy is larger than that obtained from the free inlet case for most of the experiment, in agreement with the values of E from Table 2. Comparing both panels we see the first four modes represent approximately 60% and 50% of the kinetic energy at the earlier stages for the free and grid configurations, respectively. Although after a period of $t \sim 50$ s, the grid and free inlet restricted kinetic energy percentage for $k_{\max} = 4$ represents only about 40% and 30% of the total kinetic energy, respectively. Therefore, considering only the first four modes is not enough to accurately represent the dynamics of the flow in the latter stages. This is likely a consequence of the spreading fluid being close to the walls of the container, thereby introducing boundary effects.

In Fig. 3 we observe that there is an initial period, until $t \sim 15$ s, during which the kinetic energy increases. After this point the upflow fluid has reached an initial maximum height z^i_{top}. At this stage the energy is close to 1.2% and 0.8% of the total cumulative kinetic energy for the grid and free inlet configurations, respectively. The presence of the grid nozzle enhances the mixing of the fountain with the atmosphere fluid [14], causing the rising fluid to be less dense and therefore able to accumulate more kinetic energy before achieving maximum height. Due to the same feature, z^i_{top} for the grid inlet configuration is lower than that for the free inlet configuration. After reaching z^i_{top}, in both configurations the energy is seen to achieve almost the same mean value with respect to the cumulative kinetic energy. This reveals that the fountain has reached a new top height $z_{top} < z^i_{top}$, as fluid falls and moves away from the inflow axis, at the spreading height $z_{sp} < z_{top}$. The kinetic energy oscillates around a mean energy value of 0.6%, and at $t \sim 50$ this mean value falls to about 0.5%, indicating that the maximum height z_{top} has dropped further as the horizontal spreading distance increases.

Fig. 4 compares horizontal velocity, measured by the DPIV technique with POD reconstruction, based on four modes for both configurations. The rest of the considered modes (the $M - 4$ less energetic modes) contain information on transient turbulent structures localised at different zones of the fountain. Such structures are also present at the third and fourth modes. The following section explains how they can be identified when each spatial mode and their associated energy temporal evolution are analysed together.

4.2. Spatial modes and fountain main features

The POD technique, applied on calculations from DPIV for the two experimental configurations, can be used to elucidate different spatial features of the fountains. Given that the velocity field has two components, $u(\vec{r}, t_j)$ contains $2 \times N \times M$ quantities and the spatial mode $\Phi_k(\vec{r})$ is a two-dimensional vector.

Fig. 5 shows the more energetic velocity spatial modes, or eigenvectors, $\Phi_1(\vec{r})$, $\Phi_2(\vec{r})$ and $\Phi_3(\vec{r})$ for the free and grid inlet configurations. Due to the high velocity of the fluid at the jet inlet, DPIV fields could not be measured near the fountain axis. The locations where the flow direction of the fountain has reversed can be observed, however, as shown in Fig. 5(a), (b). As described

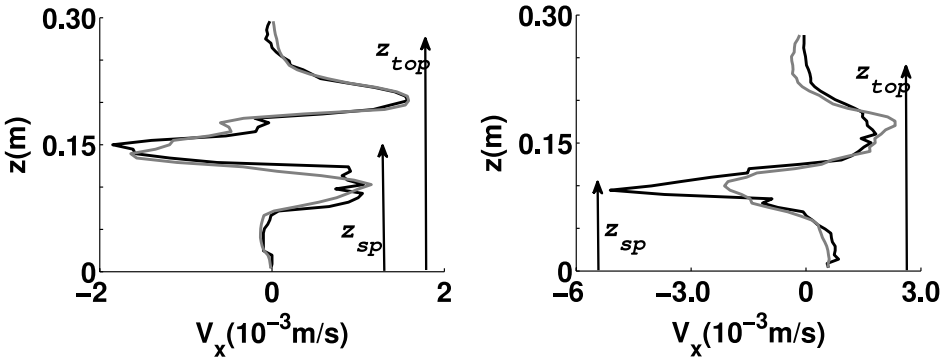

Fig. 4. Horizontal velocity v_x for all y coordinates at some fixed x on the left from the inlet location. In black and grey lines the measured and POD reconstruction fields, respectively, are represented. On the left and right, the profiles were taken at 5.6 cm and 6.1 cm, respectively, from the inlet axis at $t = 44$ s and 26 s, respectively.

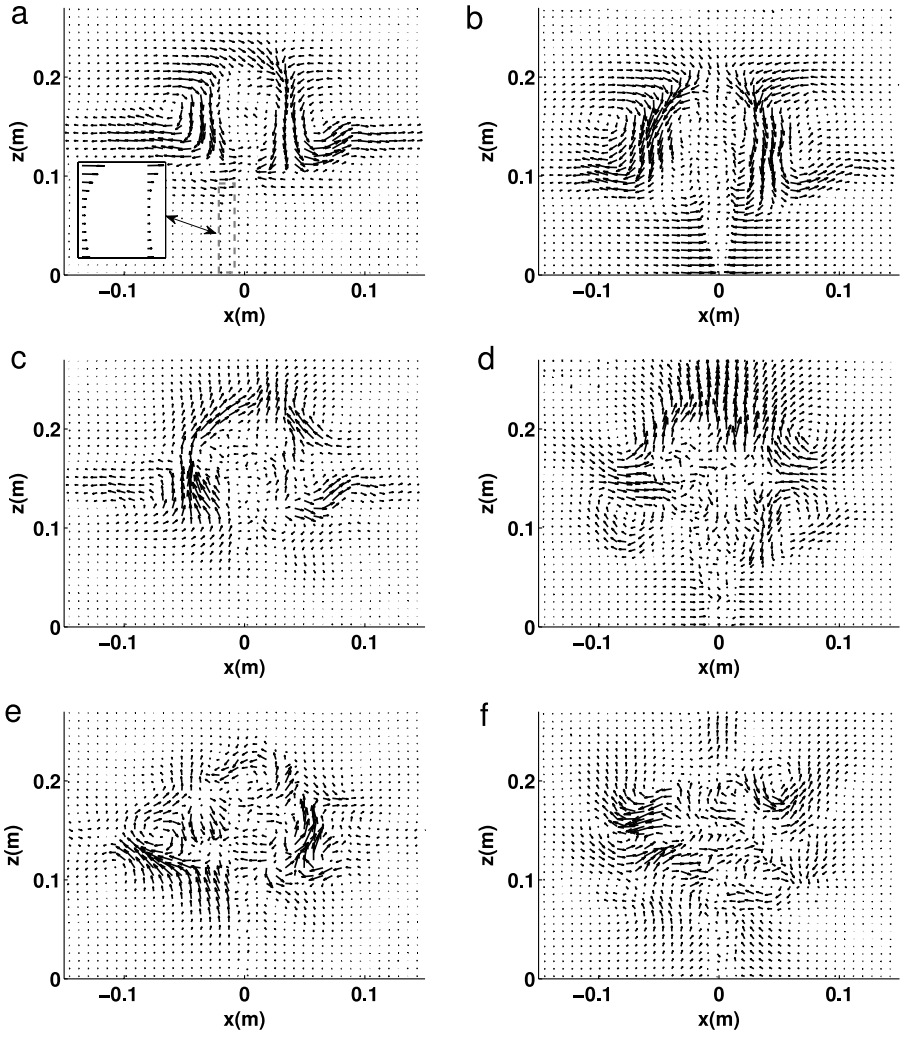

Fig. 5. Velocity fields of the first 3 spatial modes (i.e. Φ_1, Φ_2 and Φ_3), for free inlet (a), (c), (e) and grid (b), (d), (f) configurations.

by Bloomfield and Kerr [29] this forms an annular region around the jet, adjoining the upward flow. The first spatial mode also shows how fluid intrudes radially away from the fountain axis into the stratified atmosphere. The buoyancy force vanishes at a certain height, although the flow continues to fall down until the vertical momentum of the flow reduces to zero at some lower height. Temperature gradients act to elevate this height away from the bottom level, and causes the fluid to rise again. Fig. 5(a), (b) shows the natural upward vertical component of the spreading flux. While it intrudes in the environment the buoyancy force causes the flow to rise higher, until achieving a second height of zero momentum z_{sp}, where fountain and environment are at thermal equilibrium.

Beyond the identification of the spreading height, the spatial-mode analysis also shows there are two main entrainments of environment fluid [9], these being over the shear layer of the upflow and near z_{top}, due to the falling of the heavy fluid. Entrainment of the surrounding fluid into the fountain can be observed at the bottom of the fountain, in both configurations (free and grid) for the first spatial mode. Although the horizontal

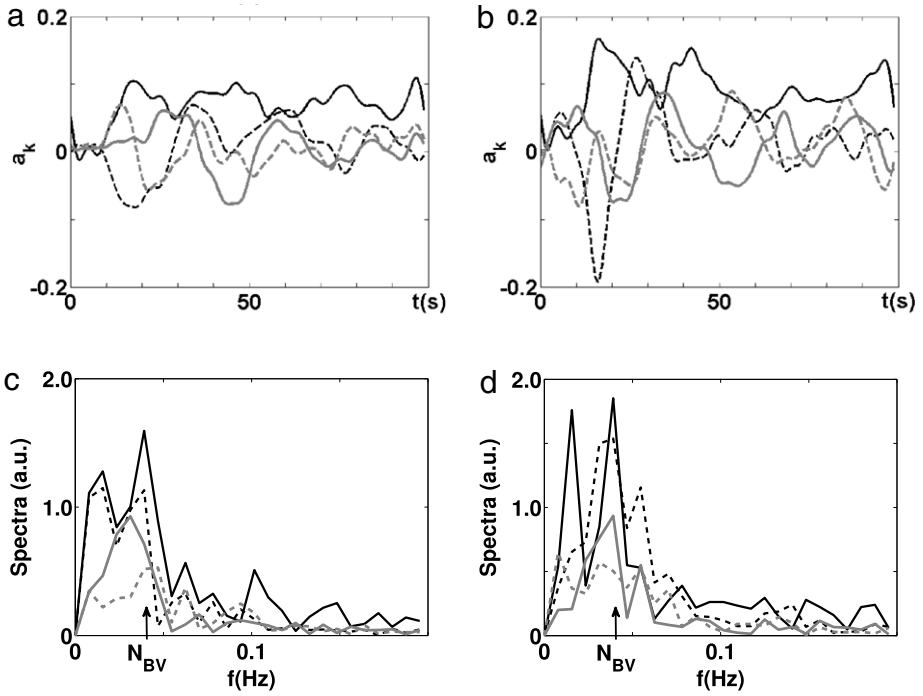

Fig. 6. Amplitude (a), (b) and Fourier spectra (c), (d) of the first temporal modes. Left and right panels correspond to the free and grid configurations, respectively. Line style and colour references are: mode 1—black continuous line; mode 2—black dashed line; mode 3—grey continuous line; mode 4—grey dashed line. N_{BV} is indicated in Figs. (c), (d).

velocity component near the source in the free inlet configuration is lower than in the grid configuration, environmental fluid (less dense) is entrained into the cold fluid jet at the entrance of both configurations, as can be seen in Fig. 5(a). The first spatial mode also shows that while a portion of the downflow spreads to the atmosphere another portion is entrained back into the upflow at the bottom of the fountain.

Fig. 5(c), (d) shows the second velocity spatial modes, which modulate the first spatial mode, improving the accuracy of the description of the real field. This mode is different for the two experimental conditions, although in both cases it reveals a strong upflow near the fountain top, supported by the level of fluctuations in z_{top}, especially at earlier stages as mentioned in Section 1. The second mode for the free inlet is found to be less symmetric than the first mode. The bottom left side of Fig. 5(c) denotes the modulation of the downflow field from the first mode by the second mode. The amplitude of the second mode oscillates around zero and fluctuations may cause detachment of some fluid from the fountain. This phenomenon can also be observed in visualisations, where small portions of dyed fluid are seen to detach from the spreading flow at the bottom left side. For the grid inlet configuration second mode, on the other hand, Fig. 5(d) suggests the presence of entrainment from the environment into the centre of the fountain, dividing the fountain in two parts. This point is revisited in the next sections.

As Fig. 5(e), (f) shows, the third (and higher order) velocity spatial modes reflect turbulent cells at the edge of the fountain, which are stable and strong initially. As the fountain dynamics evolve this spatial mode becomes weaker compared to other modes, representing new turbulent cells. As mentioned in Section 4.1, a description of these new turbulent structures requires higher order modes, however, the first three modes capture the main features characterising the two experimental configurations.

4.3. Temporal modes and energy

Fig. 6(a), (b) depicts the amplitude of the first four temporal modes. The Fourier temporal spectra of $a_k(t)$, plotted in Fig. 6(c), (d), reveal a dominant frequency of about 0.039 Hz. This main frequency coincides well with the predicted buoyancy frequency N_{BV}, (or Brunt–Väisälä frequency) given by $N_{BV} = (\alpha \Gamma g)^{1/2}$, where α is the coefficient of volumetric expansion and Γ is the temperature gradient in the vertical direction, and $g = 9.8\ \mathrm{m/s^2}$ is the gravitational acceleration. For our experimental conditions, N_{BV} was estimated to be 0.036 Hz. It was found that several frequencies that appear in the Fourier spectra of the temporal amplitudes can be related to the wave numbers of the spatial modes, through the Brunt–Väisälä dispersion relation,

$$\omega = \sqrt{\frac{k_x^2}{k_x^2 + k_z^2}} N_{BV}. \tag{8}$$

This can be interpreted as a signature of the presence of travelling waves in the dynamics of the system. We comment that the derivation of the dispersion relation Eq. (8) is usually done using non-viscous theory [30]. Starting from the linearised Navier–Stokes and heat transfer equations, it is possible to include the effects of viscosity and heat flow, to demonstrate that these effects are negligible in our experiments.

We also measured the N_{BV} frequency by applying a POD analysis to the dye visualisation data for both configurations. This was done over two small regions, one at the top of the fountain and the other over the lower layer of the dyed spreading fluid. This approach found these regions to oscillate with a frequency ∼0.031 Hz. In addition, the spatial Fourier analysis can be applied to the first four two-dimensional modes $\Phi_k(\vec{r}_i)$ to obtain the (k_x, k_z) wavevectors present at each velocity field v_x and v_z. It can then be verified whether the frequencies given by Eq. (8) are present at the unique temporal spectra of the corresponding temporal mode $a_k(t)$.

Given the temporal resolution of the DPIV, the Fourier analysis on POD provides at most five frequencies less than or equal to N_{BV}. Fig. 7 establishes that it is possible to associate several (k_x, k_z) peaks of $\Phi_k(\vec{r}_i)$ to certain frequencies present in the POD mode amplitude $a_k(t)$ for $k = 1 \ldots 4$. Fig. 7 takes account of

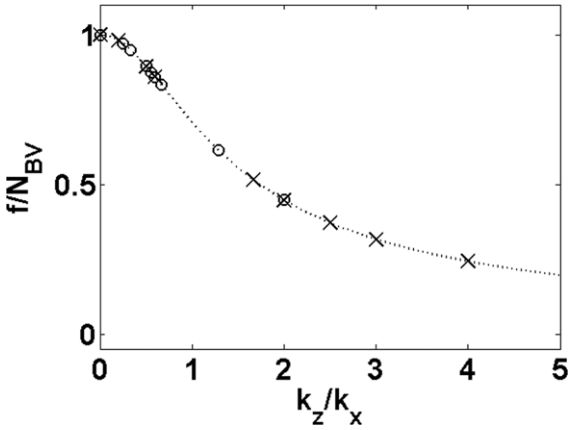

Fig. 7. Normalised frequencies as a function of the k_z/k_x ratio of the spatial modes. The dotted line corresponds to the dispersion relationship and the symbols (circles for free and crosses for grid inlet) correspond to the frequencies related to k_z/k_x ratio of the spatial modes which are in agreement with Eq. (8).

the k_z/k_x ratio, instead (k_x, k_z) pairs, because the dispersion relation depends on this ratio. More precisely, for the free (grid) configuration spatial Fourier analysis on both components of $\Phi_k(\vec{r}_i)$ identifies 17(14) pairs k_z/k_x. Out of these ratios 10(11) match the dispersion relation, because the frequency given by Eq. (8) appears at the corresponding $a_k(t)$ amplitude mode in the Fourier decomposition. Then the PODs can be identified with internal gravity waves. Nevertheless, the frequency spectra present peaks at frequencies greater than N_{BV} for the second mode and higher for the grid configuration, see Fig. 6(d), and the free inlet configuration shows the same behaviour for the fourth mode and over, see Fig. 6(c). These higher frequencies may be explained by Eq. (8), if there was a local temperature gradient at the top of the fountain [31], since in that case the cold fluid rises higher adiabatically, a thermocline emerges and, consequently, a fast variation of the density appears. This phenomenon could lead to values of N_{BV} which are locally greater than the limit imposed by the bulk external temperature gradient.

Some wave vectors obtained through the 2D-Fourier analysis of $\Phi_k(\vec{r}_i)$ predict frequencies, through the dispersion relation, that are not present in the corresponding frequency decomposition of the mode $a_k(t)$. This is, possibly, a consequence of the fact that Eq. (8) is derived from a linear approximation. Advective terms must be taken into account to assure the consistency of the whole temporal and spatial data pairs shown in Fig. 7.

4.4. Energy and velocity fields reconstruction

Beyond the Fourier analysis, the evolution of the energy modes reveals that the first spatial mode generally assumes the greatest energy values for the duration of the experiment. Figs. 9 and 10 compare the velocity fields as measured by the DPIV technique with the POD reconstruction, using the four most energetic modes, with good agreement being found.

Firstly, we analyse the results from the free configuration. In this case, there is an inward flow just above the intruding flow, as shown in Fig. 9(d). With respect to the energy, from Fig. 8(a) it is observed that $E_2(t)$ presents three main peaks and $E_3(t)$ exhibits two peaks. At $t \sim 29$ s, $E_3(t)$ is found to be slightly larger than $E_1(t)$, and $E_2(t)$ vanishes. At this instant, $a_3(t)$ is at maximum, and from Fig. 9(b) we can identify two convective cells, at the left side near the region where fountain fluid intrudes into the atmosphere. Fluid moves close to the top of the fountain to re-inject itself again to the downflow flux at different heights. At $t \sim 45$ s, $a_3(t)$ reaches a minimum and, as it can be seen in Fig. 9(d), an amount of the intruding flow returns down near to the fountain axis before being entrained with the upflow. The third mode mainly characterises the early stage fountain dynamics, while fluid is intruding the atmosphere, and afterwards becomes weaker.

Inspecting the results from the grid configuration, Fig. 8(b) shows that $E_2(t)$ presents two main peaks. At $t \sim 16$ s, $E_2(t)$ is greater than $E_1(t)$. At this instant, $a_2(t)$ reaches a minimum, leading to a stage where the fluid close to the top of the fountain is going down to re-inject to the downflow at different heights. Environment fluid entrainment is a natural consequence of downflow around the upward flow. When $a_2(t)$ reaches a maximum (at $t \sim 27$ s) a radial flow moving slightly above z_{sp} separates the fountain into two portions, one portion of the environment fluid being entrained from above and the other part from below this radial flow, similar to a jet passing an obstacle (see Fig. 5(d)). It is possible to verify that before $t \sim 50$ s, the system broadly alternates between two regimes, whose main features correspond to Fig. 10(b) and (d), and after this time the height of the just mentioned radial flow descends, and only one vortex cell is present.

5. Final remarks

In this paper, regular and turbulent structures in fountains in stratified media were identified using POD analysis of 2D-DPIV. Complementary to visualisation techniques, POD revealed the main differences between the free and grid inlet configurations.

Emphasis has been put on the capability of POD first spatial mode to reproduce, as a well-suited empirical basis, the large-scale dynamics of the fountain flow. Adding new modes to the analysis allows one to gain additional insight into specific experimental conditions. At early stages, the first few POD modes retain the main fraction of kinetic energy, thereby only requiring a small number to identify the main mechanisms of heat and mass interchange, namely entrainment between atmosphere and upflow or downflow, as shown in Fig. 5(a), (b), and convective

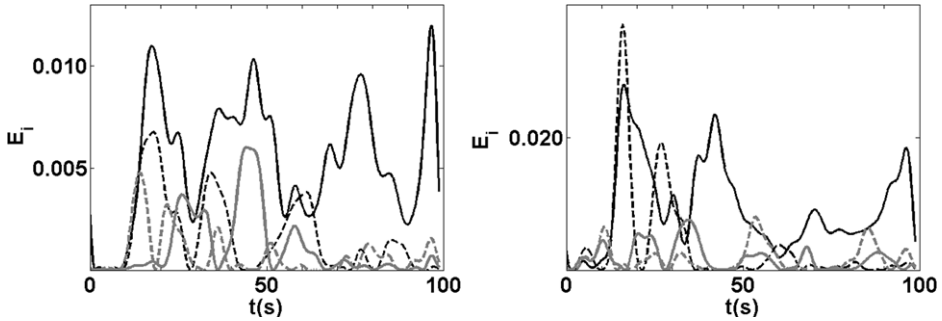

Fig. 8. Energy of the first four modes ($E_{i=1,\ldots,4}$) for the free (left) and grid (right) configurations. Line style and colour references are: mode 1—black continuous line; mode 2—black dashed line; mode 3—grey continuous line; mode 4—grey dashed line.

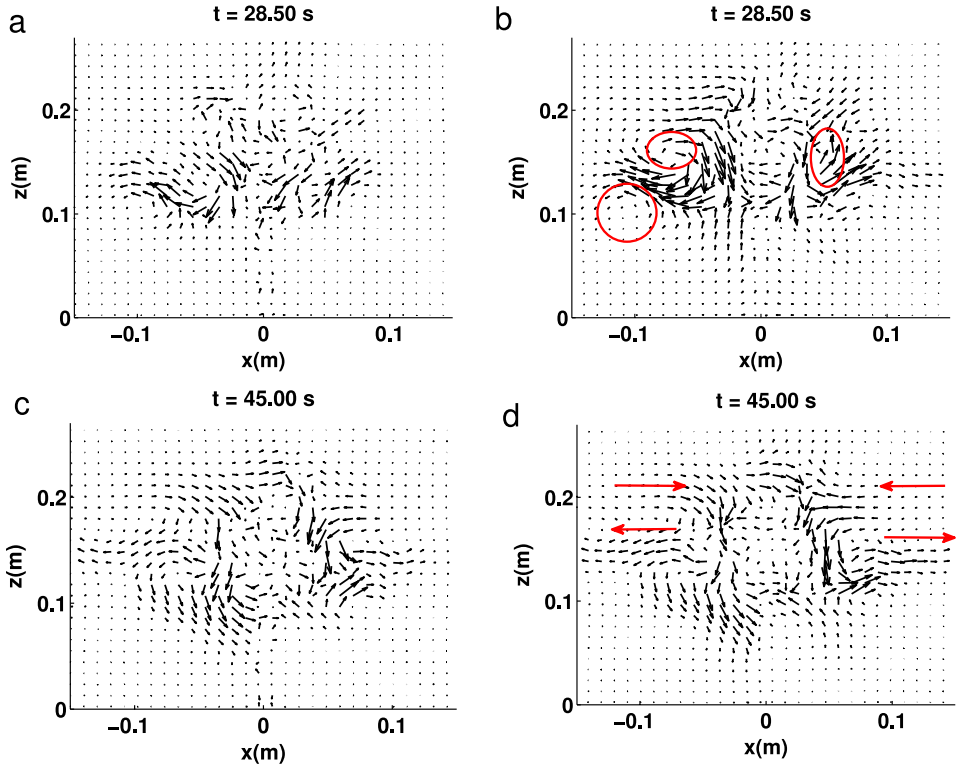

Fig. 9. Comparison between velocity fields obtained by DPIV technique (left) and the reconstruction of the fields using the four most energetic POD components (right), for the free configuration. On the right, arrows and circles remark flow direction and circular motion zones (see text).

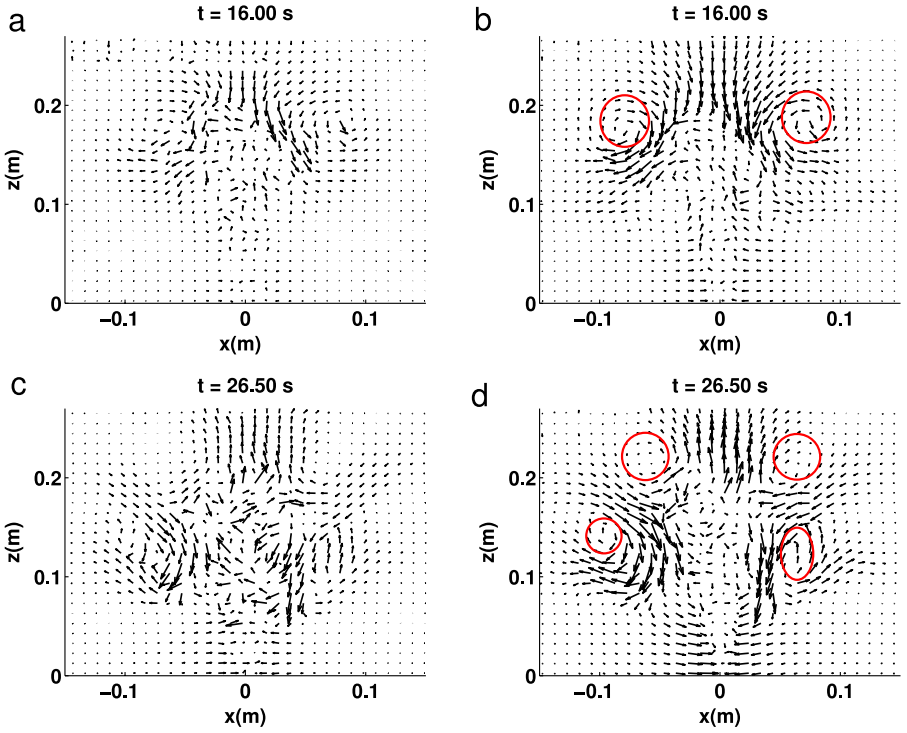

Fig. 10. Results for the grid configuration. Same references as Fig. 9.

cells like depicted in Fig. 5(e). In this way, POD spatial modes are able to precisely locate the regions in which these features occur, allowing the measurement of entrainment rates and heat transfer interchanges.

The Fourier analysis on POD modes reveals several frequencies resulting from regular and turbulent structures present at the experiments. Most of them can be related to internal gravity waves through a dispersion relation obtained by the equations governing the dynamics of stratified flows. The presence of other frequencies, however, suggests it may be necessary to extend the model by including advective nonlinear terms for a more complete description of the fluid dynamics.

Energy considerations, in association with temporal and spatial analysis, were used to identify complex periodic behaviour which requires a more detailed explanation in terms of nonlinear convection theory. In summary, POD proved to be an effective data analysis tool, allowing the quantitative characterisation of the fountain, in which several different flow regimes were found to coexist.

Acknowledgements

We acknowledge financial support from PEDECIBA, ANII and CSIC (Uruguay).

Appendix A. Supplementary material

Supplementary material related to this article can be found online at http://dx.doi.org/10.1016/j.euromechflu.2014.11.009.

References

[1] E. List, Turbulent jets and plumes, Annu. Rev. Fluid Mech. 14 (1982) 189–212.
[2] I.H. Campbell, J. Turner, Fountains in magma chambers, J. Petrol. 30 (1989) 885–923.
[3] R. Guarga, P. Mastrángelo, G. Scaglione, E. Supino, Evaluation of the SIS: a new frost protection method applied in a citrus orchard, in: Proceedings of the 9th Congress of the International Society of Citriculture, 2000.
[4] R. Guarga, Frost Protection Corp., 2013. URL: http://www.frostprotection.com.
[5] H. Augsburger, Frost control in temperate climates through dissipation of cold air, Aspects Appl. Biol. 61 (2000).
[6] M. Burke, L. Gusta, H. Quamme, C. Weiser, P. Li, Freezing and injury in plants, Annu. Rev. Plant. Physiol. 27 (1976) 507–528.
[7] R.S. Pearce, Plant freezing and damage, Ann. Bot. 87 (2001) 417–424.
[8] H. Yazdanpanah, C. Stigter, Selective inverted sink efficiency for spring frost protection in almond orchards northwest of Isfahan, Iran, Theor. Appl. Climatol. 105 (2011) 27–35.
[9] B. Morton, G. Taylor, J. Turner, Turbulent gravitational convection from maintained and instantaneous sources, Proc. R. Soc. Lond. Ser. A Math. Phys. Sci. 234 (1956) 1–23.
[10] H.C. Burridge, H.G. Hunt, The rhythm of fountains: the length and time scales of rise height fluctuations at low and high Froude numbers, J. Fluid Mech. 738 (2013) 91–119.
[11] H.C. Burridge, H.G. Hunt, The rise heights of low-and high-Froude-number turbulent axisymmetric fountains, J. Fluid Mech. 691 (2013) 392–416.
[12] O.J. Myrtroeen, H.G. Hunt, Negatively buoyant projectiles-from weak fountains to heavy vortices, J. Fluid Mech. 657 (2013) 227–237.
[13] L.J. Bloomfield, R.C. Kerr, A theoretical model of a turbulent fountain, J. Fluid Mech. 424 (2000) 197–216.
[14] D. Freire, C. Cabeza, S. Pauletti, G. Sarasúa, I. Bove, G. Usera, A.C. Martí, Effect of turbulent fluctuations on the behaviour of fountains in stratified environments, J. Phys. Conf. Ser. 246 (2010) 012015.
[15] S. Kahan, C. Cabeza, M. Pelaez, I. Bove, R. Montagne, Frequency transition of coherent structures in faraday surface waves, Int. J. Bifurcation Chaos 19 (2009) 2589–2596.
[16] J. Kostas, J. Soria, M. Chong, Particle image velocimetry measurements of a backward-facing step flow, Exp. Fluids 33 (2002) 838–853.
[17] R. Adrian, K. Christensen, Z.-C. Liu, Analysis and interpretation of instantaneous turbulent velocity fields, Exp. Fluids 29 (2000) 275–290.
[18] P. Cizmas, A. Palacios, T. O'Brien, M. Syamlal, Proper-orthogonal decomposition of spatio-temporal patterns in fluidized beds, Chem. Eng. Sci. 58 (2003) 4417–4427.
[19] P.J. Schmid, Dynamic mode decomposition of numerical and experimental data, J. Fluid Mech. 656 (2010) 5–28.
[20] A. Cenedese, P. Monti, Interaction between an inland urban heat island and a sea-breeze flow: a laboratory study, J. Appl. Meteorol. 42 (2003) 1569–1583.
[21] A. Cenedese, P. Monti, Proper orthogonal decomposition in the analysis of a laboratory simulation of land- and sea-breeze regimes, J. Fluid Mech. 510 (2004) 1–28.
[22] L. Gui, W. Merzkirch, Generating arbitrarily sized interrogation windows for correlation-based analysis of particle image velocimetry recordings, Exp. Fluids 24 (1998) 66–69.
[23] J. Westerweel, Fundamentals of digital particle image velocimetry, Meas. Sci. Technol. 8 (1997) 1379.
[24] Z.J. Taylor, R. Gurka, G.A. Kopp, A. Liberzon, Long-duration time-resolved piv to study unsteady aerodynamics, IEEE Trans. Instrum. Meas. 59 (2010) 3262–3269.
[25] Z.J. Taylor, R. Gurka, G.A. Kopp, A. Liberzon, 2010. URL: http://www.openpiv.net.
[26] P. Holmes, J.L. Lumley, G. Berkooz, Turbulence, Coherent Structures, Dynamical Systems and Symmetry, Cambridge University Press, 1998.
[27] A. Palacios, G.H. Gunaratne, M. Gorman, K.A. Robbins, Karhunen–Loève analysis of spatiotemporal flame patterns, Phys. Rev. E 57 (1998) 5958.
[28] M. Meixner, S.M. Zoldi, S. Bose, E. Schöll, Karhunen–Loeve local characterization of spatiotemporal chaos in a reaction–diffusion system, Phys. Rev. E 61 (2000) 1382.
[29] L.J. Bloomfield, R.C. Kerr, Turbulent fountains in a stratified fluid, J. Fluid Mech. 358 (1998) 335–356.
[30] I.M. Cohen, P.K. Kundu, Fluids Mechanics, Academic Press, 2004.
[31] P. Manneville, Dissipative Structures and Weak Turbulence, Springer, 1995.